Relaxation-Based Structure Refinement and Backbone Molecular Dynamics of the Dynein Motor Domain-Associated Light Chain[†]

Hongwei Wu,[‡] Martin Blackledge,[§] Mark W. Maciejewski,[‡] Gregory P. Mullen,[‡] and Stephen M. King*,[‡]

Department of Biochemistry, University of Connecticut Health Center, 263 Farmington Avenue,
Farmington, Connecticut 06030-3305, and NMR Laboratory, Institut de Biologie Structurale Jean-Pierre Ebel,
41 Rue Jules Horowitz, Grenoble 38027, France

Received August 29, 2002; Revised Manuscript Received October 30, 2002

ABSTRACT: The light chain 1 (LC1) polypeptide is a member of the leucine-rich repeat protein family and binds at or near the ATP hydrolytic site within the motor domain of the γ heavy chain from *Chlamydomonas* outer arm dynein. It consists of an N-terminal helix, a central barrel formed from six leucine-rich repeats that fold as $\beta\beta\alpha$ units, and a C-terminal helical domain that protrudes from the main axis defined by the leucine-rich repeats. Interaction with the γ heavy chain is likely mediated through a hydrophobic patch on the larger β sheet face, and the C-terminal region is predicted to insert into the dynein ATP hydrolytic site. Here we have used ^{1}H−^{15}N heteronuclear relaxation measurements obtained at 500 and 600 MHz to refine and validate the LC1 solution structure. In this refined structure, the C-terminal helix is significantly reoriented by more than 20° as compared to the control and provides a more precise understanding of the potential regulatory role of this domain. We also employed the refined structure to perform a dynamic analysis of LC1 using the 600 MHz data set. These results, which were cross validated using the 500 MHz data set, strongly support identification of the predicted LC1 binding surfaces and provide additional insight into the interaction mechanisms of leucine-rich repeat proteins.

Dyneins are microtubule-based molecular motors that transport their attached cargo toward the minus ends of microtubules. The cytoplasmic enzymes are required for vesicular transport, mitosis, maintenance of the Golgi apparatus, and nuclear envelope breakdown. Within cilia and flagella, dyneins provide the driving force for the beating movement of this organelle and thus are essential for the movement of single cells such as sperm and for fluid transport activities. Furthermore, dyneins power the vortical motion of nodal cilia and are thus required for the establishment of left−right asymmetry in the developing mammalian embryo (for reviews, see refs *1* and *2*). The outer dynein arm from flagella of *Chlamydomonas* is one of the best characterized members of this molecular motor class, and consists of more than 13 different polypeptide components with a total mass of ~2 MDa. There are three motor units [the α, β, and γ heavy chains (HCs)] within this dynein that exhibit distinct microtubule binding and translocation properties. These heavy chains are associated with different light chain proteins that apparently play a regulatory role in the control of motor function in response to various signaling inputs, and with a series of conserved components that act to attach the motor to the appropriate cellular cargo (for a recent review, see ref *3*).

Light chain 1 (LC1)[1] is a member of the SDS22^{+} subclass of the leucine-rich repeat (LRR) family and is tightly bound to the motor domain of the γ dynein HC at or near the ATP hydrolytic site (*4*). Within the flagellar axoneme, LC1 also interacts with a 45 kDa putative microtubule-binding protein (p45) that is thereby targeted to the γ HC motor domain. The NMR solution structure of LC1 (*5*) revealed that this protein consists of an N-terminal helix, a central cylindrical domain composed of six $\beta\beta\alpha$ motifs, and a C-terminal helical section that protrudes from the main protein axis. This C-terminal segment is thought to extend into the γ HC motor domain, whereas association with the γ HC is predicted to occur through a large hydrophobic patch located on one β sheet face.

Heteronuclear NMR spin relaxation is now widely used to probe the local and global dynamics of macromolecules (*6*). For backbone dynamics, an evaluation of the contributions to relaxation due to global molecular reorientation is essential, particularly in the case of anisotropic tumbling, where relaxation rates depend on the direction of the individual relaxation interaction (assumed here to follow the NH bond vector direction) relative to the rotational diffusion tensor. Fortunately, in the fast motion limit (τ < 30 ps), the R_2/R_1 ratio is dominated by the overall rotational diffusion of the molecule and can be considered independent of internal motion. Assuming that the rotational diffusion tensor is not time-dependent, we can then use the R_2/R_1 ratio to characterize molecular rotational diffusion, thereby improving the analysis of internal motions from relaxation data in more flexible regions of the molecule. The elongated shape of the

---

[†] This study was supported by Grants GM51293 (to S.M.K.) and GM63548 (to S.M.K. and G.P.M.) from the National Institutes of Health. S.M.K. is an investigator of the Patrick and Catherine Weldon Donaghue Medical Research Foundation. M.B. thanks the CNRS (France) and the Commisariat à l'Energie Atomique for financial support.

* To whom correspondence should be addressed. Telephone: (860) 679-3347. Fax: (860) 679-3408. E-mail: steve@king2.uchc.edu.

[‡] University of Connecticut Health Center.

[§] Institut de Biologie Structurale Jean-Pierre Ebel.

[1] Abbreviations: LC, light chain; LRR, leucine-rich repeat; NOE, nuclear Overhauser effect; NMR, nuclear magnetic resonance.

10.1021/bi026762j CCC: $25.00

LC1 structure, with the long axis of the molecule being nearly twice that of an orthogonal axis, suggested that anisotropic tumbling would contribute to the relaxation of ^{15}N nuclei throughout the backbone structure. Of further interest, evaluation of the structure revealed that the NH bond vectors in the β strands of the $\beta\beta\alpha$ repeat motifs are parallel to the long axis of the molecule, while the NH vectors of the α helices in these motifs are essentially perpendicular. We have exploited the orientation dependence of the NH bond vector with respect to the rotational diffusion tensor as a structural restraint to define long-range order in LC1.

The measured relaxation data can provide direct samples of the spectral density function of NH vectors along the peptide chain. In the model-free approach (*7*, *8*), the mobility of the NH vectors is characterized by an order parameter S^2 describing the amplitude of the motion and a correlation time τ_i which is the characteristic time constant of this motion. The only assumptions concerning the physical nature of the mobility are independence of internal and global motion, and the exponential nature of the overall and internal autocorrelation functions.

Here we present the relaxation-based structure refinement of the 22 kDa (198 residue) LC1 protein from the outer dynein arm of *Chlamydomonas* flagella and an analysis of the local backbone dynamics. Relaxation data, obtained at 500 and 600 MHz, from amide sites in secondary structural elements in the central region comprising the six $\beta\beta\alpha$ motifs were used to analyze the rotational diffusion of the molecule. The resulting diffusion tensor and R_2/R_1 ratios, as an additional long-range constraint, were used in the structure refinement calculation. The C-terminal helix of the structure refined using 600 MHz relaxation data has a significant reorientation of more than 20°. The 500 MHz data were used to cross validate the model-free analysis with the refined structure. The two analyses revealed consistent Lipari–Szabo parameters and indicate that LC1 is a rather rigid molecule except at the termini and within the two putative interaction surfaces.

MATERIALS AND METHODS

Sample Preparation. All NMR relaxation experiments were performed using ^{15}N-labeled samples prepared as described previously. Briefly, LC1 was expressed with an N-terminal His$_{10}$ tag using the pET16b vector. Following purification by Ni^{2+} affinity chromatography, the tag was removed by digestion with factor Xa, leaving a single additional His residue at the N-terminus. Recombinant LC1 is monomeric as determined by gel filtration chromatography and was concentrated to ~2.0 mM in 2.5 mM Tris-HCl (pH 6.7) and 100 mM NaCl with a 90% H_2O/10% D_2O mixture as the solvent.

NMR Relaxation Measurements. All relaxation experiments were carried out at 25 °C on Varian Unity-INOVA 500 and 600 MHz spectrometers each equipped with a triple-resonance pulse field *Z*-axis gradient probe and gradient amplifier. The ^{15}N R_1 and $R_{1\rho}$ relaxation rates and ^{1}H–^{15}N NOE measurements were carried out using the classical ^{1}H-detected pulse sequence based on established methods (*9*). In R_1 and $R_{1\rho}$ experiments, proton decoupling used a series of 180° pulses, spaced 5 ms apart, that were applied during the relaxation period to eliminate the contributions of dipolar cross correlation and chemical shift anisotropy to the longitudinal relaxation (*10*). ^{15}N decoupling during the acquisition was achieved using a GARP decoupling scheme. Because of the excellent water suppression achieved by use of gradients and a hard flip-back pulse (~2030 μs) at the water resonance, no additional solvent suppression or time domain deconvolution techniques were necessary. This eliminated the possible contribution of proton exchange NOEs from water. A total of 1024 (t_2) × 128 (t_1) complex points were recorded with 32 scans per increment for both R_1 and $R_{1\rho}$ experiments and 128 scans per increment for ^{1}H–^{15}N NOE experiments.

For R_1 measurements, the sampling time points were 10, 30, 60, 100, 150, 220, 300, 400, 550, 750, 1050, 1400, 1800, and 2400 ms at 500 MHz and 0, 20, 60, 100, 150, 220, 300, 400, 550, 750, 1050, 1400, 1800, 2400, and 3000 ms at 600 MHz. For $R_{1\rho}$ measurements, the sampling time points were 10, 170, 90, 250, 30, 190, 110, 290, 50, 210, 130, 350, 70, 230, 150, and 410 ms at both 500 and 600 MHz. A recycle delay of 1.5 s was employed. For $R_{1\rho}$, a ^{15}N spin-lock field was used during the relaxation decay time, with strengths of 1730 and 1320 Hz for 600 and 500 MHz fields, respectively. $R_{1\rho}$ values were corrected to compensate for resonance offset effects using eq 1.

$$R_{1\rho} = R_2 \cos^2(\theta) + R_1 \sin^2(\theta) \qquad (1)$$

where $\theta = \tan^{-1}(2\pi\Delta\nu/\gamma_N B_1)$, where $\Delta\nu$ is the resonance offset and $|\gamma_N B_1|/2\pi$ is the strength of the spin-lock field. The R_2 values were then directly extracted for each residue from $R_{1\rho}$, R_1, and θ. ^{1}H–^{15}N NOE experiments were recorded in the presence and absence of a proton saturation period of 3 s during the recycle delay, which was 5 s. The ^{1}H saturation was achieved with the use of a 120° ^{1}H pulse applied every 5 ms (*11*). Two sets of experiments were carried out and the NOE values averaged.

All spectra were processed and analyzed using the software Felix95 (Biosym Inc.) on Silicon Graphics Indigo R4400 computers. The final data sets consisted of 2048 (t_2) × 1024 (t_1) real data points after zero-filling and Fourier transformation. Linear prediction was used to extend the t_1 dimension from 128 to 256 complex points. Apodization was performed using squared sine bell window functions typically with a shift of 60°.

Relaxation Parameter Calculations. All cross-peak heights in the R_1, $R_{1\rho}$, and ^{1}H–^{15}N NOE spectra were measured using the program Felix95 (Biosym Inc.). Uncertainties in the measured peak heights were extracted from the root-mean-square baseline noise of the spectra. Differences between the values obtained from duplicate spectra were within these errors. R_1 values were calculated from the equation $I(t) = I_\infty - (I_\infty - I_0)\exp(-R_1 t)$. $R_{1\rho}$ values were calculated from the equation $I(t) = I_0 \exp(-R_{1\rho} t)$. A nonlinear least-squares fit of the experimental data was used to determine the relaxation rates for each residue. Fits were performed using the Levenburg–Marquardt algorithm (*12*) from modified scripts provided with the model-free (version 3.1) software. Uncertainties in R_1 and $R_{1\rho}$ relaxation rates were estimated by performing 500 Monte Carlo simulations based on the estimated errors in the measured peak heights (*13*, *14*). ^{1}H–^{15}N NOE values were determined from the ratio of the average peak heights in spectra recorded with proton saturation to those recorded without saturation. The uncertainties for the NOE values were calculated using the relative errors of the peaks.

Relaxation Data Analysis. The ^{15}N heteronuclear relaxation parameters R_1, R_2, and NOE depend on the spectral density function $J(\omega)$ in the following manner:

$$R_1 = d^2[J(\omega_H - \omega_N) + 3J(\omega_N) + 6J(\omega_H + \omega_N)] + c^2 J(\omega_N) \quad \text{(2a)}$$

$$R_2 = (d^2/2)[4J(0) + J(\omega_H - \omega_N) + 3J(\omega_N) + 6J(\omega_H + \omega_N) + 6J(\omega_H)] + (c^2/6)[4J(0) + J(\omega_N)] \quad \text{(2b)}$$

$$\mathrm{NOE} = 1 + d^2(\gamma_H/\gamma_N)[6J(\omega_H + \omega_N) - J(\omega_H - \omega_N)]/R_1 \quad \text{(2c)}$$

where

$$d^2 = {}^1/_{10}(\gamma_H/\gamma_N)^2(h/2\pi)^2\langle r_{NH}{}^{-3}\rangle^2$$

and

$$c^2 = {}^2/_{15}\omega_N{}^2(\sigma_{||} - \sigma_{\perp})^2$$

where h is Plank's constant, γ_H and γ_N are the gyromagnetic ratios of ^{1}H and ^{15}N, respectively, ω_H and ω_N are the Larmor frequencies of ^{1}H and ^{15}N, respectively, and r_{NH} is the internuclear distance [assumed to average to 1.01 Å (*15*)]. $\sigma_{||}$ and $\sigma_{\perp}$ are the parallel and perpendicular components, respectively, of the axially symmetric ^{15}N chemical shift tensor (approximated to −160 ppm), which is assumed to be coaxial with respect to the dipolar interaction.

In the case of isotropic tumbling of the molecule, the model-free spectral density function is defined by

$$J(\omega) = S_2{}^2\{S_1{}^2\tau_c/[1 + (\omega\tau_c)^2] + (1 - S_1{}^2)\tau'/[1 + (\omega\tau')^2]\}$$

with

$$\tau' = \tau_c\tau_i/(\tau_c + \tau_i) \quad (3)$$

where τ_c is the overall correlation time of the molecule.

Using the Lipari−Szabo model-free approach (*7*, *8*), $J(\omega)$ is derived assuming $S_2{}^2 = 1$. The generalized order parameter $S_1{}^2 = S^2$ describes the amplitude of the fast internal motion and τ' the effective correlation time for fast internal motions. If internal motion is slow, movement is characterized by $S_1{}^2 = S_s{}^2$ and τ_i, the order parameter and internal correlation time, respectively. The correlation time of the fast motion is assumed to be negligible with regard to the measured relaxation parameters which are affected only by the order parameter $S_2{}^2 = S_f{}^2$ ($S^2 = S_s{}^2S_f{}^2$) describing the rapid librational motion.

Determination of Motional Parameters. All data analysis was performed using the program TENSOR2 (*16*). The following five models were iteratively tested, starting with the simplest model and invoking more complex models until the proposed model could give rise to the measured relaxation rates within 95% confidence limits: (1) S^2, (2) S^2 and τ_i, (3) S^2 and R_{ex}, (4) S^2, τ_i, and R_{ex}, and (5) $S_f{}^2$, $S_s{}^2$, and τ_i. In model 1, motions on the fast time scale are too fast (<30 ps) to be characterized and affect R_1 and R_2 in a similar way. In model 2, internal motion is relaxation active. In models 3 and 4, R_{ex} contributes to R_2. Model 5 refers to the extended model described above.

Sets of relaxation data were fitted to dynamic models, using the optimized global correlation time (vide infra) by minimizing the function

$$\chi^2 = \sum[(R_{i,n}{}^{\mathrm{meas}} - R_{i,n}{}^{\mathrm{calc}})/\sigma_{i,n}{}^{\mathrm{meas}}]^2 \quad (4)$$

where i represents the relaxation parameters used in the calculation. $R_{i,n}{}^{\mathrm{meas}}$, $R_{i,n}{}^{\mathrm{calc}}$, and $\sigma_{i,n}{}^{\mathrm{meas}}$ are the experimental and calculated relaxation rates and the estimated experimental uncertainty of $R_{i,n}{}^{\mathrm{meas}}$, respectively. Model selection was based on 500 Monte Carlo simulations for characterizing the random variation in the fit, providing probability statistics, and estimating uncertainty. An F characteristic was used to judge the statistical significance of introducing an additional parameter to model 1. F is defined as

$$F = (N - n)(\chi_m{}^2 - \chi_n{}^2)/(n - m)\chi_n{}^2 \quad (5)$$

for the comparison of models fitting N variables with m and n parameters. In the case where the reduction of χ^2 was less than the critical value for random statistical improvement ($\alpha = 0.20$), we have rejected the more complex model and proposed the model 1 parametrization.

Anisotropic Tumbling. Fitting of the Anisotropic Rotational Diffusion Tensor. The spectral density function describing anisotropic rotational diffusion is given by

$$J(\omega) = \sum\{A_j\tau_j/[1 + (\omega\tau_j)^2]\} \quad (6)$$

where

$$A_1 = 3y^2z^2,\ A_2 = 3x^2y^2,\ A_3 = 3x^2y^2$$

$$A_{4,5} = 0.25[3(x^4 + y^4 + z^4) - 1] \pm {}^1/_{12}[\delta_x(3x^4 + 6y^2z^2 - 1) + \delta_y(3y^4 + 6x^2z^2 - 1) + \delta_z(3z^4 + 6y^2x^2 - 1)]$$

and

$$\tau_{1,2,3} = (4D_{xx} + D_{yy} + D_{zz})^{-1},\ (D_{xx} + 4D_{yy} + D_{zz})^{-1},\ (D_{xx} + D_{yy} + 4D_{zz})^{-1}$$

$$\tau_{4,5} = 6D_{\mathrm{iso}}{}^2 \pm 6(D_{\mathrm{iso}}{}^2 - L^2)^{1/2}$$

$$D_{\mathrm{iso}} = (D_{xx} + D_{yy} + D_{zz})/3$$

$$L^2 = (D_{xx}D_{yy} + D_{xx}D_{zz} + D_{yy}D_{zz})/3$$

and

$$\delta_{\mathrm{m}} = (D_{\mathrm{mm}} - D_{\mathrm{iso}})/(D_{\mathrm{iso}}{}^2 - L^2)^{1/2}$$

where m is x, y, or z and x, y, and z are the direction cosines of the N−H vector in the principal axis frame of the diffusion tensor. Six parameters (D_{xx}, D_{yy}, D_{zz}, θ, Φ, and ψ) were optimized, describing the orientation and amplitude of the principal components of the diffusion tensor in the chosen molecular frame. For axially symmetric diffusion, $D_{\perp} = D_{xx}$

$= D_{yy}$, $D_{\parallel} = D_{zz}$, t_1, t_2, and $t_3 = (6D_{\perp})^{-1}$, $(5D_{\perp} + D_{\parallel})^{-1}$, and $(2D_{\perp} + 4D_{\parallel})^{-1}$, respectively, and A_1, A_2, and $A_3 = (3 \cos^2 \alpha - 1)^2/4$, $3 \sin^2 \alpha \cos^2 \alpha$, and $^3/_4 \sin^4 \alpha$, respectively, where α is the angle between the N−H bond and the unique axis of the diffusion tensor. Four parameters were optimized ($D_{\perp}$, $D_{\parallel}$, θ, and Φ) in this case. The diffusion parameters were extracted by minimizing

$$\chi^2 = \sum[(R_2^{\mathrm{meas}}/R_1^{\mathrm{meas}} - R_2^{\mathrm{calc}}/R_1^{\mathrm{calc}})_n/\sigma_n]^2 \qquad (7)$$

where σ is the uncertainty in the experimental R_2/R_1 ratio.

The summation was performed over the residues in the secondary structural motifs. Cartesian coordinates of the appropriate vectors were taken from the LC1 Protein Data Bank file (PDB entry 1DS9). The fit of the diffusion tensor components and orientation was performed with the program TENSOR2, which uses a simulated annealing algorithm and allows for complete exploration of the available parametric space.

The program TENSOR2 also performs Monte Carlo simulations to evaluate the uncertainty of the fitted diffusion parameters and to test the significance of the fit against the estimated experimental error. Here, 1000 simulated sets of R_1 and R_2 values for each residue were selected from Gaussian noise distributions of width σ_R and centered on the optimal rates back-calculated from the best-fit anisotropic diffusion parameters.

The axially symmetric and asymmetric fits require four- and six-parameter fits, respectively, to model the rotational diffusion. It is therefore important to test the significance of the improved fit to ensure that the reduced χ^2 is not simply due to the introduction of supplementary parameters into the model. This was examined by calculating the random statistical improvement achieved when noise simulations assuming axial symmetry were fitted using an asymmetric model. Distinction between the different diffusion models was achieved by calculating the function F (vide supra) to test the justification of including more parameters in the fit. If the F statistic is greater than a given threshold, then the improved model is statistically relevant. This can also be expressed as a probability p that the improvement is due to random fluctuation.

Extraction of Global Correlation Time. The global isotropic correlation time was optimized by treating residues that exhibited no obvious signs of relaxation active mobility on the basis of heteronuclear ^{1}H−^{15}N NOE values at 500 and 600 MHz (NOE > 0.65). The diffusion tensor was optimized using the algorithm presented above (eq 7), assuming isotropic motion.

Anisotropy and Internal Mobility. The orientation and components of the diffusion tensor were introduced into the first term of the general spectral density function:

$$J(\omega) \approx S^2 \sum A_j \tau_j/[1 + (\omega\tau_j)^2] + (1 - S^2)\tau'/[1 + (\omega\tau')^2] \qquad (8)$$

with

$$\tau'^{-1} = 6D + \tau_{\mathrm{i}}^{-1}$$

This definition was used to characterize the local mobility in terms of the Lipari−Szabo formalism. Fast internal motion [$\tau_{\mathrm{i}} \ll (6D)^{-1}$] is assumed to be independent of overall rotational tumbling and is thus analogous to the isotropic Lipari−Szabo model-free approach. Statistical testing of the significance of the derived models was carried out using the same criteria for model selection as in the isotropic case.

Structure Refinement Using Heteronuclear Relaxation. All structure calculations were performed using the program SCULPTOR (Structure Calculation Using Long-range, Paramagnetic, Tensorial and Orientational Restraints) (*17*), an in-house program interfaced to the molecular dynamics program DISCOVER (MSI Inc., San Diego, CA), written specifically to exploit orientation-dependent NMR interactions as long-range structural restraints. SCULPTOR allows a flexible approach for exploiting ^{15}N relaxation within molecular dynamics structure calculations. Tensor parameters are treated independently from the molecule of interest, and eigenvalues and eigenvectors can thus be manipulated independently.

Structure Calculation Protocol. The program DISCOVER version 2.98 was modified to include the relaxation constraint as an explicit target potential in the classical potential energy function of the AMBER4 force field (*18*)

$$E_{R_2R_1} = k_{R_2R_1}(R_2^{\mathrm{meas}}/R_1^{\mathrm{meas}} - R_2^{\mathrm{calc}}/R_1^{\mathrm{calc}})^2/\sigma^2 \qquad (9)$$

Two values for the uncertainty σ_{ij} were used during the calculation; in the initial, tensor determination part of the protocol, residue-specific experimental errors for the relaxation rates were used, whereas during the structure refinement period, a uniform weighting was then applied throughout the primary sequence. To avoid distortion of local geometry during structure refinement, and to ensure reorientation of structural elements of correct covalent geometry, force constants defining peptide planarity and local valence angles were also increased.

The rotational diffusion tensor was determined using amide sites in the $\beta\beta\alpha$ barrel region of the molecule, the internal mobility of which was negligible on the basis of heteronuclear NOE at 500 and 600 MHz (NOE > 0.65). In SCULPTOR, the rotational diffusion tensor **D** is described by four separate molecules representing the orientation (molecule 1) and the three axes (molecules 2−4) of the tensor. Two complete sets of ^{15}N relaxation data were available from ^{1}H frequencies of 500 and 600 MHz. We used the 600 MHz data in the structure refinement protocol, reserving the 500 MHz data as a cross validation control for the resulting structures.

During the initial period, designed to determine the optimal tensor, the coordinates of the protein were fixed, and the orientation and eigenvalues of the tensor were optimized by minimizing the energy function given by eq 9 with the four molecules representing **D** completely free to evolve. This process is identical to the tensor determination using TENSOR2, but essentially embeds this tensor in the structure calculation. The molecules representing the tensor were then tethered to these eigenvalues during the rest of the structure refinement calculation, during which the molecular coordinates were optimized with respect to the standard NOE and dihedral angle restraints and relaxation rate data. During this period, R_2/R_1 values from throughout the molecule were used, provided that the heteronuclear NOE showed no evidence of internal motion.

The quartic repulsion term in the force field used 0.825 of the standard van der Waals radii. All molecular dynamics protocols used weak coupling to a temperature bath unless otherwise stated. Nonbonded interactions employed a sigmoid cutoff function, which started at 6.5 Å, so that no interactions beyond 8.0 Å were taken into consideration. A time step of 1.0 fs was used throughout the calculation.

The molecule was initially equilibrated at 600 K for 5 ps using direct velocity scaling, followed by a 7.5 ps sampling period. The system was slowly cooled to 100 K over a period of 10 ps and energy minimized in the same force field. This ensemble was taken to represent the final structure in agreement with all experimentally measured data.

The entire calculation, including determination of the diffusion tensor, was repeated for all the different conformers in the previously determined NMR ensemble (*5*). This set of calculations was repeated using no relaxation data, to test for force field- or protocol-dependent effects, and served as a control for the calculations that included the relaxation data.

Quantification of Structural Differences in the C-Terminal Region. To quantify the different orientation of structural motifs present in the C-terminal domain in the diverse ensembles, the following procedure was adopted. The axis of a helix was defined as the direction of the average vector over all backbone (N, C_α, and C) atoms along the peptide chain for the relevant residues. The angle between this vector and the equivalent vector of the structure closest to the mean coordinates was then calculated over the whole ensemble. This was repeated relative to the same helix in the structure closest to the mean from the corresponding comparative ensemble (control or relaxation-refined).

Coordinates. The coordinates and constraints for the control and relaxation-refined ensembles of LC1 structures have been deposited in the Protein Data Bank (entry 1M9L).

RESULTS

^{15}N NMR Data Analysis. A ribbon diagram of the original mean LC1 structure (*5*) is shown in Figure 1. This extended molecule consists of an N-terminal helix, six $\beta\beta\alpha$ repeats that fold as a right-handed spiral to form the central barrel, and a C-terminal helical domain that extends from the main protein axis. For ^{15}N relaxation measurements, 191 of the 198 protonated backbone nitrogens of LC1 were available. Residues that could not be detected included five prolines (P35, P36, P151, P174, and P183), E29, and the N-terminal M1. The measured ^{15}N relaxation rates R_1 and R_2 and ^{1}H−^{15}N NOE and order parameter (S^2) values, at 500 and 600 MHz, are shown in Table 1. The average values and errors calculated by Monte Carlo simulations were 1.37 ± 0.07 and 1.08 ± 0.08 s^{-1} for R_1, 18.68 ± 0.88 and 21.52 ± 1.08 s^{-1} for R_2, 0.76 ± 0.03 and 0.77 ± 0.03 for the NOE at 500 and 600 MHz, respectively. On average, the calculated errors represent approximately 5% of the measured values. The mean R_1 rate at 500 MHz is ~1.26 times faster than at 600 MHz. For all other α helices, except α helix 7 whose axis is parallel to the molecular axis, the local averaged R_1 rates are higher than the average value for the entire molecule (Figure 2a). Conversely, for all β strands, the local averaged R_1 rates are lower than the whole average value at both field strengths. The last six amide sites of helix 9, located in the C-terminal domain, have high R_1, low R_2, and low NOE values compared with other secondary structural elements (Figure 2a−c), indicating that this region may be more flexible than the main barrel domain.

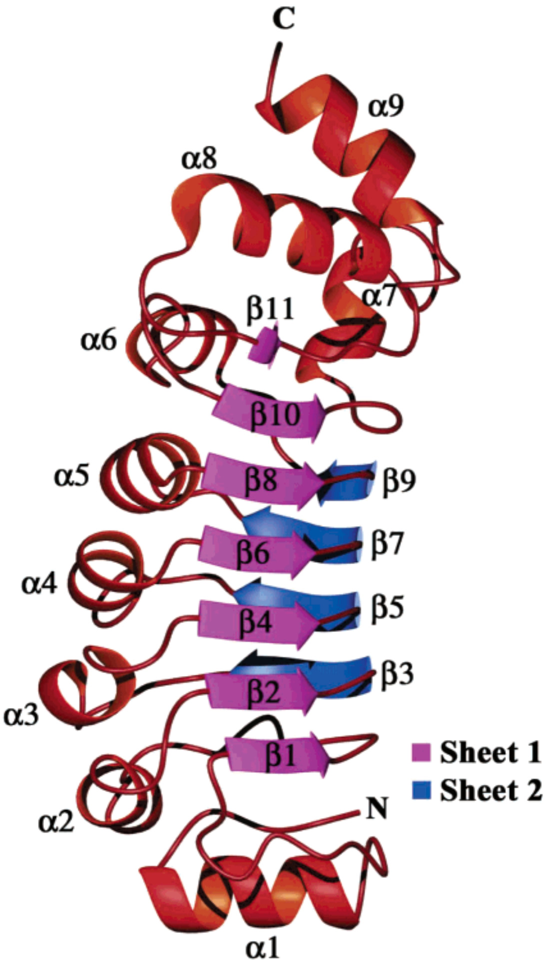

FIGURE 1: Ribbon diagram of the original mean LC1 structure. The C-terminal α helical domain protrudes from the main protein axis defined by the central barrel formed from six LRRs. The β strands comprising sheets 1 and 2 are magenta and blue, respectively.

R_2/R_1 Ratios. R_2/R_1 ratios are dependent on the orientation of the relaxation mechanisms with respect to the rotational diffusion tensor of the molecule. Hydrogen bonds formed from the N−H vectors of the β-sheets are approximately parallel to the main axis of LC1, whereas those of the α helices (excluding helix 7) are nearly perpendicular to the main LC1 axis. Thus, the internuclear N−H vectors in the different structural motifs of LC1 are almost orthogonal (Figure 1). The cyclic dependence of R_1 and R_2 (less evident) along the primary sequence appears to be due to the presence of the strand−strand−helix repeat with the NH vectors in the helices and strands sampling near-perpendicular directions. Consequently, the R_2/R_1 ratio varies with respect to the primary sequence of the protein, with all β strands exhibiting larger R_2/R_1 ratios than the α helices (with the exception of helix 7) (Figure 2d and Table 1). The R_2/R_1 ratios for helix 7 are relatively high because the axial orientation of this helix and its N−H vectors are nearly parallel to the main LC1 axis. Four residues (S56, G78, S101, and S123) exhibit significantly lower R_2/R_1 ratios than their neighbors within the β strands, as their N−H vectors are

Table 1: ^{15}N Relaxation Rates, NOEs, and Order Parameter Values at 500 and 600 MHz[a]

500 MHz					600 MHz				
residues	R_1	R_2	NOE	S^2	residues	R_1	R_2	NOE	S^2
all (2−198)	1.37 ± 0.07	18.68 ± 0.88	0.76 ± 0.03	0.94 ± 0.02	all (2−198)	1.08 ± 0.08	21.52 ± 1.08	0.77 ± 0.03	0.95 ± 0.03
core (6−192)	1.36 ± 0.07	19.11 ± 0.88	0.79 ± 0.03	0.96 ± 0.02	core (6−192)	1.07 ± 0.08	22.00 ± 1.07	0.80 ± 0.03	0.97 ± 0.03
helices 1−9	1.46 ± 0.06	18.26 ± 0.48	0.76 ± 0.02	0.94 ± 0.02	helices 1−9	1.15 ± 0.07	21.01 ± 0.60	0.78 ± 0.02	0.95 ± 0.03
strands 1−11	1.25 ± 0.06	20.23 ± 0.82	0.82 ± 0.02	0.96 ± 0.02	strands 1−11	0.99 ± 0.06	22.89 ± 0.90	0.80 ± 0.02	0.98 ± 0.02
H1 (7−16)	1.44 ± 0.06	18.13 ± 0.39	0.79 ± 0.02	0.95 ± 0.02	H1 (7−16)	1.13 ± 0.10	20.88 ± 0.41	0.78 ± 0.01	0.98 ± 0.01
H2 (41−47)	1.62 ± 0.07	18.01 ± 0.41	0.77 ± 0.01	0.98 ± 0.01	H2 (41−47)	1.30 ± 0.05	21.10 ± 0.83	0.82 ± 0.01	0.92 ± 0.08
H3 (66−70)	1.51 ± 0.07	18.29 ± 0.77	0.74 ± 0.02	0.96 ± 0.01	H3 (66−70)	1.17 ± 0.06	20.58 ± 0.46	0.72 ± 0.02	0.95 ± 0.01
H4 (88−95)	1.45 ± 0.08	18.68 ± 0.40	0.77 ± 0.01	0.97 ± 0.01	H4 (88−95)	1.12 ± 0.08	20.82 ± 0.39	0.76 ± 0.01	0.96 ± 0.03
H5 (108−117)	1.49 ± 0.04	18.21 ± 0.64	0.72 ± 0.02	0.91 ± 0.02	H5 (108−117)	1.16 ± 0.06	20.50 ± 0.69	0.81 ± 0.03	0.93 ± 0.03
H6 (130−137)	1.43 ± 0.04	18.87 ± 0.43	0.80 ± 0.02	0.97 ± 0.01	H6 (130−137)	1.11 ± 0.03	21.66 ± 0.57	0.81 ± 0.01	0.99 ± 0.01
H7 (152−157)	1.25 ± 0.05	20.35 ± 0.54	0.82 ± 0.02	0.96 ± 0.01	H7 (152−157)	1.01 ± 0.11	23.79 ± 0.67	0.85 ± 0.01	0.99 ± 0.02
H8 (162−173)	1.42 ± 0.06	18.10 ± 0.30	0.79 ± 0.02	0.95 ± 0.03	H8 (162−173)	1.12 ± 0.09	21.32 ± 0.81	0.82 ± 0.02	0.93 ± 0.05
H9 (187−197)	1.50 ± 0.05	15.68 ± 0.40	0.63 ± 0.01	0.83 ± 0.01	H9 (187−197)	1.20 ± 0.04	18.40 ± 0.63	0.66 ± 0.02	0.87 ± 0.02
B1 (27−30)	1.31 ± 0.08	19.61 ± 1.03	0.83 ± 0.03	0.96 ± 0.03	B1 (27−30)	1.02 ± 0.03	22.61 ± 0.68	0.80 ± 0.03	0.99 ± 0.01
B2 (52−55)	1.30 ± 0.02	20.33 ± 0.49	0.81 ± 0.01	0.97 ± 0.01	B2 (52−55)	1.03 ± 0.05	22.62 ± 0.55	0.83 ± 0.01	0.98 ± 0.02
B3 (57−60)	1.29 ± 0.08	19.84 ± 0.69	0.84 ± 0.03	0.95 ± 0.02	B3 (57−60)	1.00 ± 0.05	23.87 ± 1.18	0.82 ± 0.03	1.00 ± 0.02
B4 (74−77)	1.21 ± 0.06	20.65 ± 1.17	0.83 ± 0.04	0.96 ± 0.03	B4 (74−77)	0.97 ± 0.08	22.25 ± 1.92	0.79 ± 0.03	0.96 ± 0.04
B5 (79−82)	1.25 ± 0.08	20.15 ± 1.53	0.83 ± 0.02	0.97 ± 0.04	B5 (79−82)	0.98 ± 0.04	22.78 ± 0.88	0.79 ± 0.06	0.99 ± 0.02
B6 (97−100)	1.12 ± 0.06	21.20 ± 0.93	0.85 ± 0.03	0.93 ± 0.01	B6 (97−100)	0.97 ± 0.17	23.12 ± 0.75	0.83 ± 0.02	0.98 ± 0.02
B7 (102−105)	1.28 ± 0.11	20.55 ± 1.13	0.87 ± 0.03	0.96 ± 0.02	B7 (102−105)	0.94 ± 0.06	23.36 ± 0.89	0.81 ± 0.03	0.96 ± 0.02
B8 (119−122)	1.16 ± 0.04	21.24 ± 0.23	0.82 ± 0.01	0.97 ± 0.01	B8 (119−122)	0.90 ± 0.02	23.78 ± 0.22	0.78 ± 0.00	0.99 ± 0.01
B9 (124−126)	1.23 ± 0.05	20.42 ± 0.33	0.77 ± 0.03	0.96 ± 0.01	B9 (124−126)	1.01 ± 0.01	23.18 ± 0.88	0.82 ± 0.03	0.99 ± 0.02
B10 (144−147)	1.28 ± 0.07	20.28 ± 1.13	0.78 ± 0.02	0.98 ± 0.03	B10 (144−147)	0.99 ± 0.05	23.05 ± 1.54	0.75 ± 0.03	0.99 ± 0.03
B11 (178 and 179)	1.27 ± 0.00	18.29 ± 0.33	0.73 ± 0.01	0.92 ± 0.01	B11 (178 and 179)	1.05 ± 0.04	21.18 ± 0.44	0.78 ± 0.01	0.96 ± 0.01
C1 (2−6)	1.61 ± 0.06	11.92 ± 0.46	0.08 ± 0.02	0.59 ± 0.01	C1 (2−6)	1.37 ± 0.06	13.60 ± 0.54	0.29 ± 0.02	0.60 ± 0.01
C2 (17−26)	1.29 ± 0.05	18.11 ± 1.03	0.81 ± 0.02	0.93 ± 0.02	C2 (17−26)	1.02 ± 0.04	21.14 ± 0.88	0.78 ± 0.01	0.96 ± 0.02
C3 (31−40)	1.34 ± 0.09	19.21 ± 0.70	0.82 ± 0.02	0.97 ± 0.02	C3 (31−40)	1.08 ± 0.06	22.96 ± 1.63	0.79 ± 0.02	0.99 ± 0.02
C4 (48−51)	1.34 ± 0.09	20.25 ± 1.33	0.77 ± 0.04	1.00 ± 0.03	C4 (48−51)	1.03 ± 0.16	22.81 ± 2.34	0.83 ± 0.05	1.00 ± 0.05
C5 (61−65)	1.34 ± 0.05	18.82 ± 0.47	0.79 ± 0.02	0.97 ± 0.01	C5 (61−65)	1.02 ± 0.04	21.71 ± 0.25	0.85 ± 0.02	0.98 ± 0.01
C6 (71−73)	1.45 ± 0.12	20.76 ± 1.73	0.84 ± 0.05	1.00 ± 0.04	C6 (71−73)	1.25 ± 0.07	24.90 ± 2.34	0.75 ± 0.03	0.94 ± 0.06
C7 (83−87)	1.28 ± 0.06	18.88 ± 1.08	0.79 ± 0.01	0.93 ± 0.03	C7 (83−87)	1.03 ± 0.05	21.46 ± 0.46	0.72 ± 0.02	0.96 ± 0.02
C8 (106 and 107)	1.24 ± 0.01	20.07 ± 1.14	0.81 ± 0.03	0.95 ± 0.00	C8 (106 and 107)	1.13 ± 0.23	22.51 ± 1.49	0.71 ± 0.02	0.97 ± 0.04
C9 (127−129)	1.36 ± 0.08	19.55 ± 0.24	0.87 ± 0.03	0.98 ± 0.01	C9 (127−129)	1.05 ± 0.03	24.36 ± 0.39	0.83 ± 0.02	1.00 ± 0.01
C10 (138−143)	1.31 ± 0.07	18.55 ± 0.92	0.77 ± 0.03	0.95 ± 0.02	C10 (138−143)	0.98 ± 0.03	21.81 ± 1.48	0.81 ± 0.04	0.97 ± 0.02
C11 (148−150)	1.23 ± 0.05	19.17 ± 1.96	0.80 ± 0.04	0.92 ± 0.04	C11 (148−150)	0.97 ± 0.09	21.72 ± 2.06	0.89 ± 0.05	0.98 ± 0.04
C12 (158−161)	1.24 ± 0.02	19.59 ± 0.20	0.79 ± 0.00	0.96 ± 0.00	C12 (158−161)	0.94 ± 0.03	23.03 ± 0.38	0.80 ± 0.00	0.99 ± 0.01
C13 (175−177)	1.32 ± 0.04	19.68 ± 1.54	0.83 ± 0.05	0.98 ± 0.02	C13 (175−177)	0.92 ± 0.03	21.93 ± 0.98	0.79 ± 0.04	0.97 ± 0.02
C14 (180−186)	1.37 ± 0.06	18.77 ± 0.96	0.81 ± 0.03	0.96 ± 0.02	C14 (180−186)	1.05 ± 0.06	21.00 ± 0.73	0.74 ± 0.02	0.96 ± 0.02

[a] The R_1 and R_2 rates and NOE and order parameter (S^2) values for individual regions of secondary structure are indicated. The residues comprising the helices (H), strands (B), and coil (C) regions are indicated in parentheses. Also shown is the standard deviation for each value.

nearly perpendicular to the main axis. All these residues are at the junction between two adjacent β strands.

Overall Correlation Time. If we consider residues which have NOE values greater than 0.65, the global correlation time (τ_c) for the LC1 molecule assuming isotropic tumbling is $(14.0 \pm 0.1) \times 10^{-9}$ and $(13.6 \pm 0.1) \times 10^{-9}$ s^{-1} as calculated from the 600 and 500 MHz data, respectively. Although these values are, in general, consistent with a molecule of 198 residues (see ref *19*), in both cases use of an isotropic rotational diffusion model violated expected confidence limits as compared to the estimated experimental uncertainty (Tables 2 and 7), and are therefore statistically rejected [χ_{exp}^2 (=215) > $\chi_{0.05}^2$ (=187) and χ_{exp}^2 (=284) > $\chi_{0.05}^2$ (=192), respectively]. This is not surprising in view of the anisotropic nature of the inertia tensor. A full analysis of the diffusion tensor was therefore undertaken.

Determination of the Rotational Diffusion Tensor. One hundred sixty-eight and one hundred sixty ^{15}N relaxation rates from the 500 and 600 MHz data sets, respectively, were identified as exhibiting negligible internal mobility on the basis of heteronuclear ^{1}H−^{15}N NOE measurements. To establish how well the measured data fit with the structures generated from classical NMR data, the rotational diffusion tensor parameters were determined using the program TENSOR2. When those residues exhibiting negligible internal motion were fitted to the complete structure, this approach led to a less anisotropic tensor [$D_{xx} = (1.08 \pm 0.03) \times 10^{-7}$ s^{-1}, $D_{yy} = (1.16 \pm 0.03) \times 10^{-7}$ s^{-1}, and $D_{zz} = (1.34 \pm 0.03) \times 10^{-7}$ s^{-1}] than suggested from the NMR structure and a statistically insignificant model (Table 2) as measured from 1000 noise-based Monte Carlo simulations [χ_{exp}^2 (=186) > $\chi_{0.05}^2$ (=179)]. The low qualitative and quantitative level of this fit may derive from inaccurate long-range order, which, in the NMR ensemble, is defined only by short-range structural data. This could lead to the incorrect relative orientation of vectors in different parts of the molecule, and a subsequent inability to fit all orientations to the same model. Consequently, we employed a less ambiguous approach that concentrated on a local structural motif the internal geometry of which was confidently known.

In the case of LC1, the fold of the central $\beta\beta\alpha$ barrel region was determined by short-range interstrand NOEs and side chain−side chain interhelical distances, and was therefore precisely defined. This structural motif has also been found to be highly similar with a region of U2A′ from the human spliceosome (*20*) and internalin B (InIB) from the cell wall of *Listeria monocytogenes* (*21*). The rmsds for the superimposed backbone atoms of the $\beta\beta\alpha$ regions of LC1 and these two molecules are 0.702 and 1.242 Å, respectively, as determined by MOLMOL. Relaxation data from amide

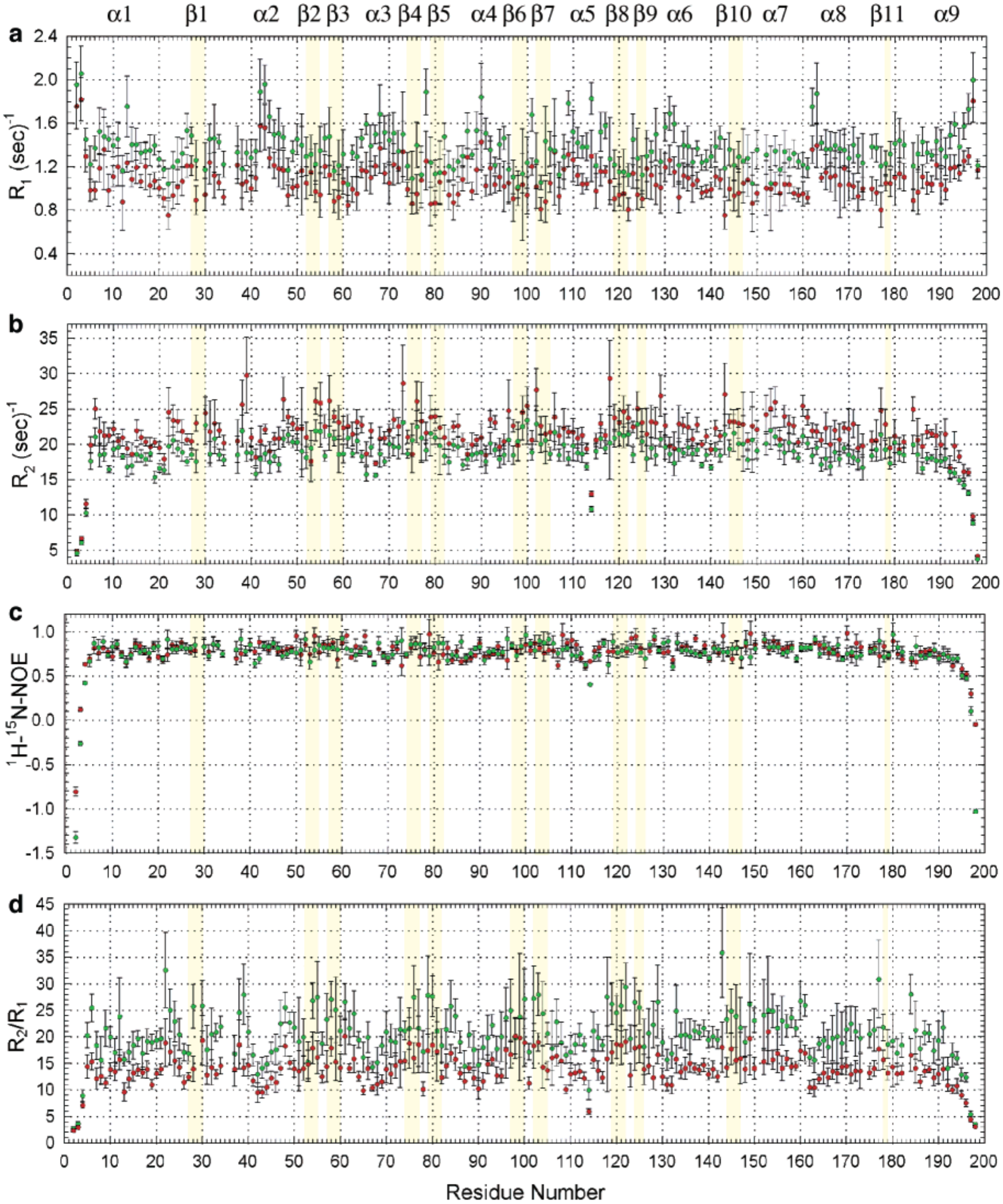

FIGURE 2: R_1 (a) and R_2 (b) relaxation rates, $^1H-^{15}N$ NOEs (c), and R_2/R_1 ratios (d) for the LC1 protein at 500 and 600 MHz for each residue. Data obtained at 500 and 600 MHz are indicated as red and green circles, respectively. Residues located within defined secondary structure elements are shown in block colors (light blue for α helix and light yellow for β strand). The individual secondary structure elements are labeled at the top.

sites in secondary structural elements in the central region of this motif (D41−K126) were therefore used to analyze the rotational diffusion of the molecule with greater confidence. The internuclear N−H vectors of this restricted region sample a broad angular space, as the barrel is composed of both extended strands and α helices arranged in an approximately continuous spiral. Not surprisingly, the fit to this region of the molecule is more convincing based on the statistical analysis [χ_{exp}^2 (=46) < $\chi_{0.05}^2$ (=67); Table 2]. The rotational diffusion tensor has axes [$D_{xx} = (0.96 \pm 0.21) \times 10^{-7}$ s^{-1}, $D_{yy} = (1.21 \pm 0.19) \times 10^{-7}$ s^{-1}, and $D_{zz} = (1.45 \pm 0.47) \times 10^{-7}$ s^{-1}], suggesting a significantly rhombic tensor. Although the central barrel is axially symmetric, the overall tensor is rhombic due to the nonaxial orientation of the C-terminal domain. The inertia tensor, the rotational diffusion tensor, and the angles between them were calculated using TENSOR2 (Figure 3). The rotational diffusion tensor is inversely related to the corresponding inertia tensor. For LC1, the D_{zz} axis of the diffusion tensor is almost collinear (4.3° difference) with the I_{zz} axis of the inertia tensor as expected. Dispersion of the axial orientations of the rotational diffusion tensor due to experimental uncertainty was calcu-

Table 2: Diffusion Tensor Parameters from R_2/R_1 Ratios (600 MHz)

1DS9 (160 sites fitted)

tensor[a]	D_{xx} ($\times 10^7$ s^{-1})[b]	D_{yy} ($\times 10^7$ s^{-1})	D_{zz} ($\times 10^7$ s^{-1})	α (deg)[c]	β/ϕ (deg)	γ/θ (deg)	χ_{exp}^2	$\chi_{0.05}^2$ [d]
axial $\mathbf{m}_1$	1.12 ± 0.01[e]	1.12 ± 0.01	1.35 ± 0.03	–	67.5 ± 8.5	−73.7 ± 8.8	186	183
axial $\mathbf{m}_2$	1.07 ± 0.03	1.25 ± 0.02	1.25 ± 0.02	–	83.8 ± 10.8	18.4 ± 10.8	195	182
asymmetric	1.08 ± 0.03	1.16 ± 0.03	1.34 ± 0.03	1.4 ± 24.8	66.7 ± 10.9	−71.1 ± 7.8	184	181

Barrel Region of 1DS9 (55 sites fitted)

tensor[f]	D_{xx} ($\times 10^7$ s^{-1})	D_{yy} ($\times 10^7$ s^{-1})	D_{zz} ($\times 10^7$ s^{-1})	α (deg)	β/ϕ (deg)	γ/θ (deg)	χ_{exp}^2	$\chi_{0.05}^2$
axial $\mathbf{m}_1$	1.07 ± 0.03	1.07 ± 0.03	1.55 ± 0.10	–	75.6 ± 11.9	−76.7 ± 9.0	48.3	65.4
axial $\mathbf{m}_2$	0.86 ± 0.07	1.33 ± 0.04	1.33 ± 0.04	–	−88.3 ± 8.4	12.7 ± 8.5	46.8	66.5
asymmetric	0.96 ± 0.21	1.21 ± 0.19	1.45 ± 0.47	9.2 ± 35.8	67.6 ± 38.4	−76.1 ± 18.7	46.0	63.9

[a] All calculations were performed using the program TENSOR2. Parameter uncertainties were taken from the mean and standard deviations of Monte Carlo simulations. The isotropic model gives the following: $\tau_c = (13.98 \pm 0.08) \times 10^{-9}$ s^{-1} with $\chi_{\text{exp}}^2 = 215$ compared to $\chi_{0.05}^2 = 187$. As a result, this model is rejected. [b] $D_\perp$ and $D_\parallel$ are shown here as D_{xx}, D_{yy}, and D_{zz} for direct comparison with the generally asymmetric diffusion tensor. For the prolate approximation ($\mathbf{m}_1$), $D_\parallel = D_{zz}$ and $D_\perp = D_{xx} = D_{yy}$; for the oblate approximation ($\mathbf{m}_2$), $D_\parallel = D_{xx}$ and $D_\perp = D_{zz} = D_{yy}$. [c] Angles (α, β, and γ) describe the orientations of $\mathbf{D}$ in the NMR structure frame. $D_{xx} < D_{yy} < D_{zz}$. For axial symmetry, the polar angles θ and ϕ are given. [d] $\chi_{0.05}^2$ in this and other diffusion tensor descriptions refers to the $\alpha = 0.05$ confidence limit for the relevant fit derived from 1000 noise-based Monte Carlo simulations. [e] The quoted uncertainty is based on Monte Carlo noise simulations; in all structural ensembles, the dispersion due to structural variation was smaller than dispersion from the relaxation data. [f] Parameter uncertainties were taken from mean and standard deviations of Monte Carlo simulations. The isotropic model gives the following: $\tau_c = (13.77 \pm 0.14) \times 10^{-9}$ s^{-1} with $\chi_{\text{exp}}^2 = 93.1$ compared to $\chi_{0.05}^2 = 71.1$. As a result, this model is rejected.

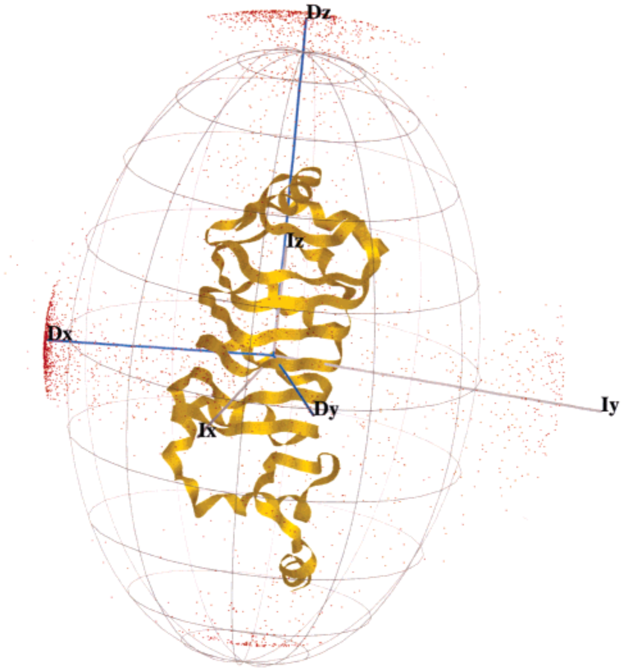

FIGURE 3: Relative orientations of the three principal axes of the asymmetric diffusion tensor and the inertia tensor of the LC1 molecule. The relative angles between inertia and diffusion tensor axes are as follows: $I_x/D_x = 70.0°$, $I_y/D_y = 70.1°$, and $I_z/D_z = 4.3°$. These tensors were calculated from the 600 MHz R_2/R_1 data using coordinates from the barrel region of 1DS9 (55 sites fitted). One thousand Monte Carlo simulations reproducing experimental uncertainty were used to estimate dispersion in the amplitude and orientation of the principal components of the diffusion tensor relative to the three-dimensional structure of the protein. The red points represent the direction of the three axes for each simulation, and the blue lines indicate the optimal diffusion tensor. The inertia tensor is represented with gray lines.

Table 3: Structural and Tensorial Statistics from Relaxation Refinement of LC1

	N[a] ensemble, 15 refined	N[a] ensemble, 15 control[b]
E_{phys} (kcal/mol)[c]	81 ± 7	122 ± 15
$E_{\text{L-J}}$ (kcal/mol)[d]	−495 ± 8	−480 ± 18
$E_{\text{noe/dihe}}$ (kcal/mol)[e]	54.3 ± 1.6	41.9 ± 3.4
violated NOE (>0.3 Å)	0	0
violated dihedral (>3°)	0	0
E_{R_2/R_1} (kcal/mol)[f]	321 ± 11	

[a] Number of structures taken into account. Statistics are given for final ensembles of 15 structures comprising the lowest-energy structure refined from each of the initial conformers. [b] Identical calculation performed in the absence of relaxation restraints. [c] Physical energy of the structure as measured using the standard AMBER4 force field. No electrostatic terms were used, and a nonbond interaction cutoff of 10 Å was applied. [d] Nonbond energy of the structures as measured using the standard Lennard-Jones potential. No electrostatic terms were used, and a nonbond interaction cutoff of 10 Å was applied. [e] Calculated assuming $k_{\text{noe}} = 50.0$ kcal mol^{-1} Å^{-2}. [f] Calculated assuming $k_{R_2/R_1} = 1.0$ kcal/mol.

Table 4: Structural Dispersion of the Control and Refined Ensembles

	refined[a]	control[b]
pairwise C_α rmsd (Å)	0.76 ± 0.16	0.98 ± 0.15
rmsd vs. average C_α (Å)	0.51 ± 0.09	0.67 ± 0.09

[a] Average pairwise rmsd calculated over all C_α atoms. [b] This refers to the no-relaxation restraints control calculation. The average pairwise rmsd over the same atoms *between* this ensemble and the initial ensemble (PDB entry 1DS9) is 1.03 ± 0.16 Å, and *within* the 1DS9 ensemble 0.95 ± 0.10 Å. The backbone atom dispersion with respect to the mean coordinates is 0.68 ± 0.15 Å for the 1DS9 ensemble. The SCULPTOR-refined and initial ensembles are therefore essentially indistinguishable.

lated directly from Monte Carlo simulations (Figure 3). The D_{zz} and D_{xx} components are relatively well defined; the D_{yy} component is less well defined.

Structure Refinement Using ^{15}N Relaxation as Constraints. The rotational diffusion tensor was assumed to provide a reasonable description of molecular tumbling and consequently was used in the structure refinement steps of the calculation. A two-step SCULPTOR protocol was developed; the first step allowed the diffusion tensor to adopt values coherent with the central barrel structure as described above so that, in the second step, data from throughout the molecule could be used to refine the relative orientation of different regions relative to this tensor. Tables 3−5 provide a summary

Table 5: Comparison of the Control and Refined Structures

		interconformational angle θ (deg)[a]	
		refined ensemble	control ensemble
orientation of the C-terminal helix 9[b]	relative to R_2/R_1-refined average[c]	2.4 ± 1.7	28.1 ± 2.4
	relative to control average[d]	25.4 ± 3.8	5.0 ± 3.3
orientation of helix 8[e]	relative to R_2/R_1-refined average	4.2 ± 2.6	7.5 ± 2.7
	relative to control average[e]	10.1 ± 3.7	4.1 ± 2.0

[a] The angle θ is defined as the angle (in degrees) between the axes of the named helices in two different structures. In each case, the average over the ensemble compared to the structure closest to the average coordinates of the relevant ensemble is given. The coordinates of each ensemble were initially superimposed on the average coordinates using the backbone barrel region comprising residues 41−147. [b] The C-terminal helix orientation was measured over the comparatively rigid residues D187−V194 (approximately two turns). [c] Conformation closest to the average in the relaxation-refined ensemble. [d] Conformation closest to the average in the control ensemble. [e] Helix 8 is comprised of residues T162−L173.

of the structural statistics, dispersion, and comparison following the relaxation refinement of LC1. Superposition of the backbone atoms of the two ensembles of refined and control structures is shown in Figure 4a. The resultant refined structural ensemble is of course very similar to the initial structural ensemble, as all of the short-range conformational restraints are common to both calculations. Comparison of the initial (*5*) and control ensembles showed no significant differences in violations despite the different force fields and structure calculation programs. Compared to the control ensemble, the refined ensemble is energetically more stable and shows less dispersion (Tables 3 and 4). The control and refined ensembles are essentially indistinguishable from the initial ensemble based on the backbone C_α atom rmsd with respect to their respective mean coordinates (for the LC1 initial, control, and refined ensembles, the average rmsds are 0.68 ± 0.15, 0.67 ± 0.09, and 0.51 ± 0.09, respectively). There is, however, a significant difference in the relative geometry of the C-terminal region in the control and relaxation-refined models (Figure 4b−d). In particular, the orientation of helix 8 differs by almost 10° and the orientation of helix 9 by more than 20° between the two ensembles (Table 5). The R_2/R_1 ratios from the six terminal amide sites were all excluded from the refinement procedure on the basis of significant internal motion. The difference in the orientation of helix 9 is therefore the result of refinement against six R_2/R_1 ratios from the first half of the helix, which shows no signs of internal mobility, the reoriented helix 8, which makes hydrophobic (and NOE) contacts with helix 9, and the R_2/R_1 ratios present in the intervening coil region (P174−V186).

Validation of the Refined Model Using the 500 MHz Data Set. To validate the relaxation-refined model, we compared the resultant structure with the independently measured experimental data from 500 MHz (Table 6). This resulted in a significant improvement in the fit using all nonmobile residues from throughout the structure ($\chi_{\mathrm{exp}}^2 = 136$ for the refined structure compared to a value of 246 for the control structure; see Tables 6 and 7), and eigenvalues and eigenvectors similar to those determined from the identical analysis performed using the 600 MHz data [$D_{xx} = (0.93 \pm 0.03) \times 10^{-7}$ s^{-1}, $D_{yy} = (1.20 \pm 0.03) \times 10^{-7}$ s^{-1}, and $D_{zz} = (1.56 \pm 0.04) \times 10^{-7}$ s^{-1} for 500 MHz data and $D_{xx} = (0.85 \pm 0.04) \times 10^{-7}$ s^{-1}, $D_{yy} = (1.18 \pm 0.03) \times 10^{-7}$ s^{-1}, and $D_{zz} = (1.53 \pm 0.04) \times 10^{-7}$ s^{-1} for 600 MHz data; see Tables 6 and 8]. This cross validation therefore demonstrates a significant improvement of the relaxation-refined ensemble over the initial (and control) structures. The diffusion tensor found from this analysis is also qualitatively in agreement with the global shape of the molecule, as the major axis D_{zz} of the diffusion tensor is close (4.6° difference) to the orientation of the equivalent inertia tensor axis I_{zz} of the final structure (Figure 5).

The relaxation-refined structure was not represented in the initial ensemble determined previously (*5*), and it is possible that conformational space was inadequately sampled by that ensemble. However, in the current study, the conformational space of the R_2/R_1 refined and control structures (the latter was calculated using the same parameter set but not incorporating the relaxation data) overlaps, and members of the control ensemble, which exhibits a broader rmsd, indeed sample conformations close to that of the refined structure. However, most members of the control ensemble do not adopt this conformation as there is no energetic reason to do so.

Anisotropic Rotational Tumbling. Model-Free Approach. The anisotropic diffusion tensor model was then used to determine the internal mobility of the LC1 molecule in solution using the program TENSOR2, which allows anisotropic rotational tumbling to be accounted for in the model-free spectral density function. This analysis was performed using both 500 and 600 MHz relaxation data. The S^2, τ_{i}, R_{ex}, and fitted model for each residue are shown in Figures 6 and 7. In the 600 MHz data set, there are six residues assigned to model 6, indicating that they are unable to be adequately fitted by any of the five models. For the 500 MHz data set, there are two residues not fitted by any model. The average order parameter S^2 value is 0.95 ± 0.03 for the 600 MHz data (0.94 ± 0.02 for the 500 MHz data; see Table 1). The N-terminal region (residues 2−6) and the C-terminal final six amide sites (residues 193−198) are relatively more flexible and have lower average S^2 values, 0.60 ± 0.01 and 0.67 ± 0.01 for the 600 MHz data, respectively (0.59 ± 0.01 and 0.62 ± 0.01 for the 500 MHz data, respectively). Helix 5 (residues 108−117) also has an S^2 value at both field strengths (0.93 ± 0.03 at 600 MHz and 0.91 ± 0.02 at 500 MHz) lower than the overall average order parameter, suggesting that it is more flexible than other helices.

Overall, the LC1 molecule is rather rigid, and there is both qualitative and quantitative agreement between the two sets of internal mobility parameters. For example, the N-terminal and C-terminal residues exhibit very similar Lipari−Szabo parameters in the two analyses (see the Supporting Information). Also, helix 5 (residues 108−117) exhibits a lower S^2 in both cases. As a further indication of the quality of fit for internal mobility, a number of residues (A2, K3, A4, I13, V21, S67, N87, L114, E132, D140, N159, and A195−G198) showing more complex motions have very similar internal

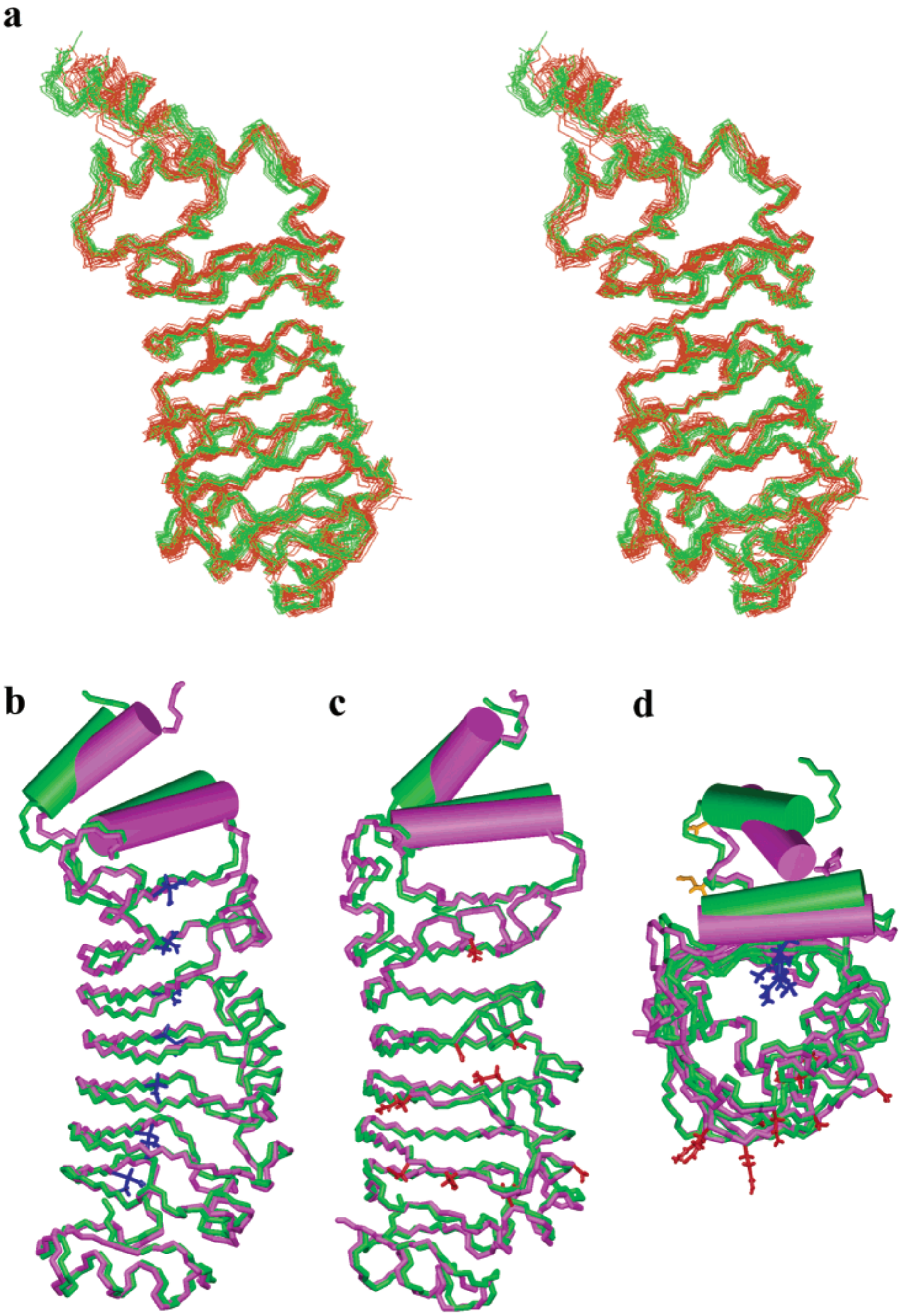

FIGURE 4: (a) Stereoview of the LC1 backbone calculated with (green) and without (red-orange) ^{15}N 600 MHz R_2/R_1 ratio relaxation constraints. The traces from 15 simulated annealing structures are superimposed for each ensemble. (b−d) Diagram of the averaged refined structure (green trace and cylinders) calculated using R_2/R_1 ratios at 600 MHz overlaid on the averaged control structure (magenta trace and cylinders) obtained without relaxation data. The orientation of panel c is rotated ∼180° with respect to the *y*-axis of panel b. A view down the central barrel of LC1 is shown in panel d. Side chains of V28, L53, L75, L98, L120, L145, and L179 located in sheet 1, which protrude inside the barrel and exhibit lower order parameters than their neighbors, are shown in blue (b and d). Side chains (red) of residues (T43, E61, K62, S67, K83, E88, S107, S109, and E132) with lower order parameters located on the opposite face extend into the solvent (c and d). Side chains (orange) of two residues (M182 and D185) located in the loop region of residues 182−185 also have lower order parameters. The rmsds for the backbone (residues D41−L147) alignment of the structures in panels a and b−d are 0.533 and 0.580 Å, respectively. The C-terminal helix 9 in the refined structure is significantly reoriented by >20° compared with the control; helix 8 is reoriented by ∼10°.

correlation times (τ_i) and order parameters (S^2) in the two analyses. Almost all residues exhibiting more complex motion and very similar Lipari−Szabo parameters are located in or near the α helical regions and not in the two β sheets.

DISCUSSION

Here, we have used ^{15}N relaxation data to refine the solution structure of the dynein motor domain-associated protein LC1 and to describe the backbone dynamics of this molecule. These results represent the first dynamics analysis of a LRR protein, and have intriguing implications for the role of this protein in dynein biology and for the mechanism by which LC1 interacts with other axonemal components.

Anisotropic Tumbling. LC1 is a highly extended molecule and is not expected to tumble isotropically. From the R_2/R_1 distribution over the entire LC1 sequence, we observed that

Table 6: Diffusion Parameters from 500 MHz R_2/R_1 Data Using Coordinates Refined Using 600 MHz Relaxation Data (168 sites fitted)

tensor[a]	D_{xx} ($\times 10^7$ s^{-1})	D_{yy} ($\times 10^7$ s^{-1})	D_{zz} ($\times 10^7$ s^{-1})	α (deg)	β/ϕ (deg)	γ/θ (deg)	χ_{exp}^2	$\chi_{0.05}^2$
axial $\mathbf{m}_2$	0.95 ± 0.03	1.37 ± 0.02	1.37 ± 0.02	–	62.4 ± 3.0	−2.3 ± 3.4	196	191
axial $\mathbf{m}_1$	1.08 ± 0.01	1.08 ± 0.01	1.53 ± 0.03	–	−86.1 ± 3.5	85.0 ± 3.0	168	191
asymmetric	0.93 ± 0.03	1.20 ± 0.03	1.56 ± 0.03	31.4 ± 4.6	−82.1 ± 4.3	84.1 ± 3.0	136	188

[a] Parameter uncertainties were taken from means and standard deviations of Monte Carlo simulations. The isotropic model gives the following: $\tau_c = (13.55 \pm 0.06) \times 10^{-9}$ s^{-1} with $\chi_{\mathrm{exp}}^2 = 284$ compared to $\chi_{0.05}^2 = 192$. As a result, this model is rejected.

Table 7: Axially Symmetric and Fully Anisotropic Diffusion Parameters from 500 MHz R_2/R_1 Data Using Coordinates from the Control Ensemble (168 sites fitted)

tensor[a]	D_{xx} ($\times 10^7$ s^{-1})	D_{yy} ($\times 10^7$ s^{-1})	D_{zz} ($\times 10^7$ s^{-1})	α (deg)	β/ϕ (deg)	γ/θ (deg)	χ_{exp}^2	$\chi_{0.05}^2$
axial $\mathbf{m}_2$	1.11 ± 0.02	1.29 ± 0.02	1.29 ± 0.02	–	41.3 ± 7.2	−9.8 ± 14.7	263	188
axial $\mathbf{m}_1$	1.16 ± 0.01	1.16 ± 0.01	1.38 ± 0.03	–	87.0 ± 7.2	86.9 ± 7.6	249	188
asymmetric	1.12 ± 0.02	1.20 ± 0.03	1.38 ± 0.03	−62.3 ± 19.4	87.1 ± 6.8	84.2 ± 8.9	246	186

[a] Parameter uncertainties were taken from means and standard deviations of Monte Carlo simulations. The isotropic model gives the following: $\tau_c = (13.55 \pm 0.06) \times 10^{-9}$ s^{-1} with $\chi_{\mathrm{exp}}^2 = 284$ compared to $\chi_{0.05}^2 = 192$. As a result, this model is rejected.

Table 8: Diffusion Parameters from 600 MHz R_2/R_1 Data Using Coordinates Refined Using 600 MHz Relaxation Data (160 sites fitted)

tensor[a]	D_{xx} ($\times 10^7$ s^{-1})	D_{yy} ($\times 10^7$ s^{-1})	D_{zz} ($\times 10^7$ s^{-1})	α (deg)	β/ϕ (deg)	γ/θ (deg)	χ_{exp}^2	$\chi_{0.05}^2$
axial $\mathbf{m}_2$	0.86 ± 0.04	1.35 ± 0.02	1.35 ± 0.02	–	66.4 ± 3.0	−0.9 ± 3.1	118	185
axial $\mathbf{m}_1$	1.03 ± 0.01	1.03 ± 0.01	1.53 ± 0.04	–	89.1 ± 3.7	89.6 ± 3.0	107	186
asymmetric	0.85 ± 0.04	1.18 ± 0.03	1.53 ± 0.04	26.7 ± 4.6	−85.9 ± 5.3	88.4 ± 3.1	75	183

[a] Parameter uncertainties were taken from means and standard deviations of Monte Carlo simulations. The isotropic model gives the following: $\tau_c = (13.98 \pm 0.08) \times 10^{-9}$ s^{-1} with $\chi_{\mathrm{exp}}^2 = 215$ compared to $\chi_{0.05}^2 = 188$. As a result, this model is rejected.

the R_2/R_1 ratios obviously varied between the different secondary structure elements. This also implies that LC1 does not tumble isotropically. The diffusion tensor calculated from the nonmobile amide sites from throughout the molecule did not fit well to the relaxation data, and resulted in a model which is statistically unacceptable based on estimated experimental uncertainty. This may be due to the inability of short-range (principally NOE) data to define long-range order in extended molecules such as LC1. We therefore chose to analyze the central barrel region of LC1 which is structurally well-defined and obtained a significantly rhombic diffusion tensor. Using TENSOR2, we also obtained two orthogonal minimum unique axes for prolate and oblate spheroids that are statistically significant and acceptable models. Previously, it has been reported that care must be taken when interpreting results assuming axially symmetric tumbling because in the case of full anisotropy two minima may be present in the parametric space (*17*, *22*). In general, the presence of two equally significant minima implies that the rotational diffusion tensor is significantly rhombic, and so the axially symmetric approximation brings no significant improvement to the analysis. Thus, in this study we considered the fully anisotropic diffusion tensor of LC1. From the 600 MHz data set using relaxation-refined coordinates and if axially symmetric tumbling is assumed, two minima are statistically acceptable with the error function χ_{exp}^2 for the prolate case being smaller than that of the oblate spheroid. However, χ_{exp}^2 for the fully asymmetric diffusion tensor is much smaller and statistically significant (less than $\chi_{0.05}^2$). This tensor provides a much closer fit to the experimentally measured parameters.

Comparison of Structural and Dynamic Information. Refinement of the complete LC1 structure against R_2/R_1 ratios using the diffusion tensor determined from the central barrel section resulted in a slight but concerted reorientation of the C-terminal region of the molecule compared to the initial

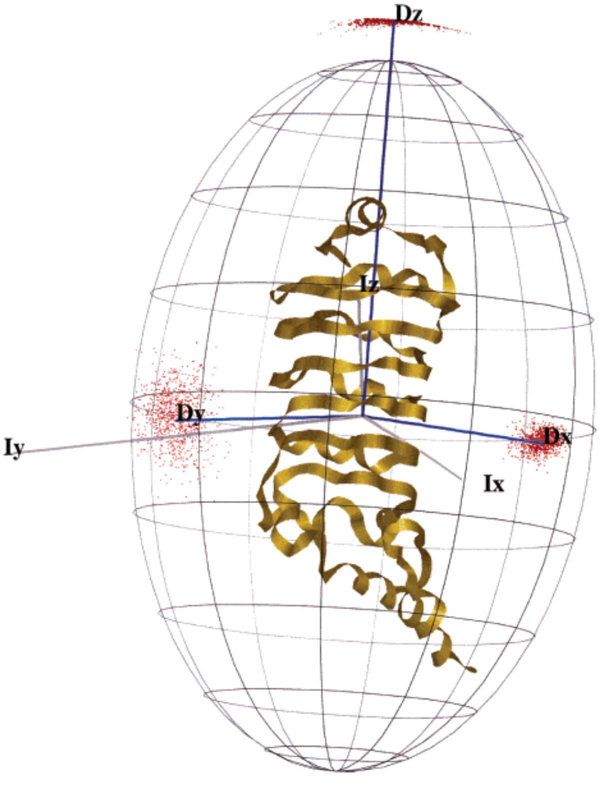

FIGURE 5: Relative orientations of the three principal axes of the asymmetric diffusion tensor and the inertia tensor. The relative angles between inertia and diffusion tensor axes are as follows: $I_x/D_x = 37.3°$, $I_y/D_y = 37.4°$, and $I_z/D_z = 4.6°$. These were calculated from the 500 MHz R_2/R_1 data using coordinates refined using 600 MHz relaxation data (168 sites fitted). One thousand Monte Carlo simulations reproducing experimental uncertainty were used to estimate the dispersion in the amplitude and orientation of the principal components of the diffusion tensor relative to the three-dimensional structure of the protein. The red points represent the axes from the simulations. The blue and gray lines represent the optimal diffusion tensor and inertia tensor, respectively.

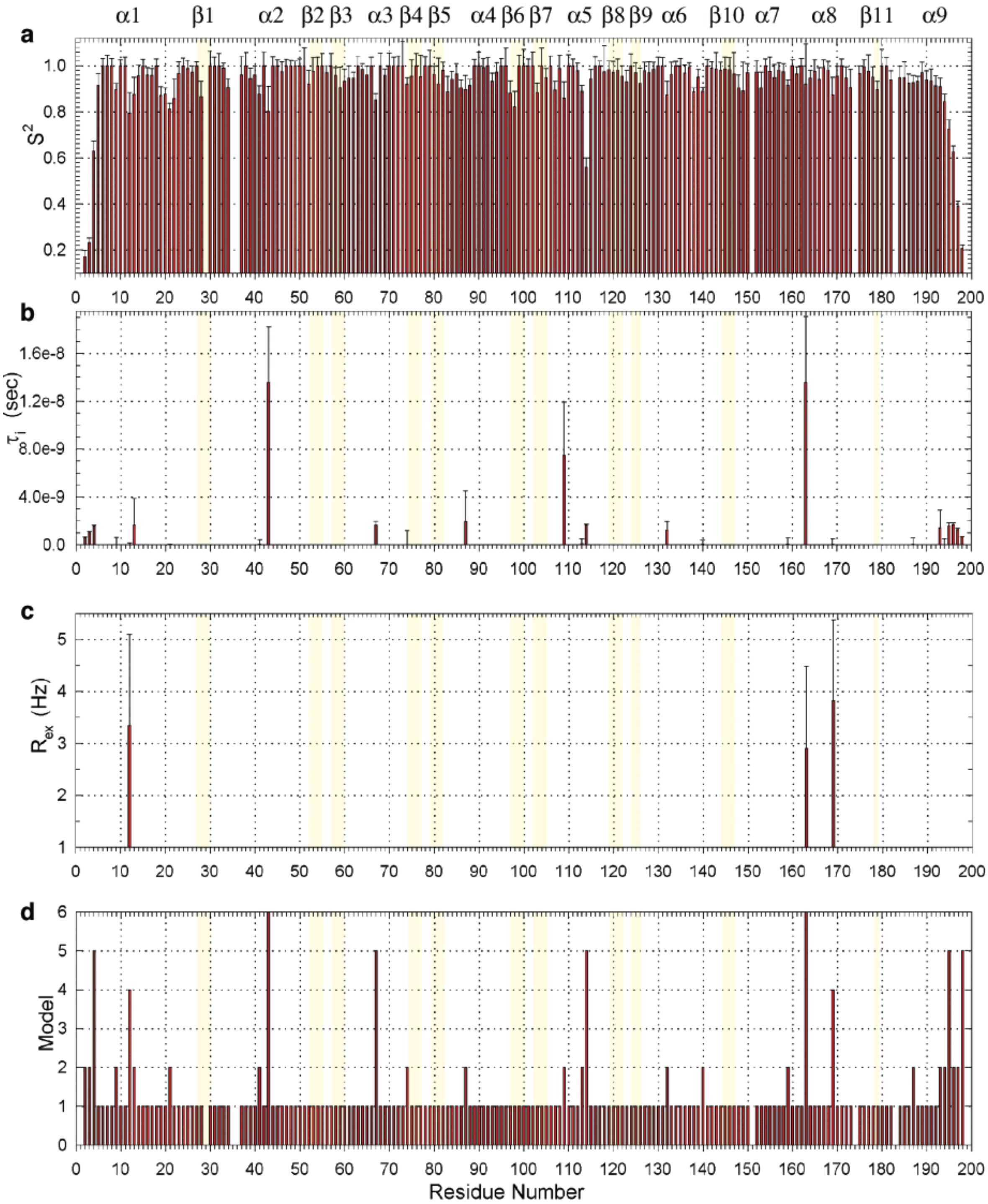

FIGURE 6: Dynamic parameters calculated from the 500 MHz data for each residue of the LC1 molecule assuming a fully anisotropic rotational diffusion tensor. Error ranges are indicated where appropriate. (a) Order parameter S^2. (b) Internal correlation time τ_i (seconds). (c) Exchange contribution R_{ex} (hertz). (d) The model that can account for the measured relaxation rates of each residue is indicated [(1) S^2, (2) S^2 and τ_i, (3) S^2 and R_{ex}, (4) S^2, τ_i, and R_{ex}, (5) S_f^2, S_s^2, and τ_I, and (6) not fitted by models 1−5]. Residues located within defined secondary structure elements are shown in block colors (light blue for α helix and light yellow for β strand). The individual secondary structure elements are labeled at the top.

calculation which used no long-range restraints. This refined conformation is in agreement with both short- and long-range restraints. To check the model further, we reserved the relaxation data measured at 500 MHz for independent cross validation. The fit of these data to the refined model resulted in a clear improvement in the statistical analysis, and a diffusion tensor very similar to that determined from the 600 MHz data, thus demonstrating the significance of the structure refinement. This validation justified our use of this model in analyzing the internal mobility of LC1 using both relaxation data sets.

A ribbon representation of the LC1 molecule colored using the order parameter S^2 as a scale to visualize the differential mobility is shown in Figure 8. Most residues in β sheet 1 have almost fully limited high-frequency backbone motion (high order parameters). There are many hydrophobic residues exposed in this β sheet, which is thought to interact with the motor domain of the γ dynein heavy chain (*5*). On

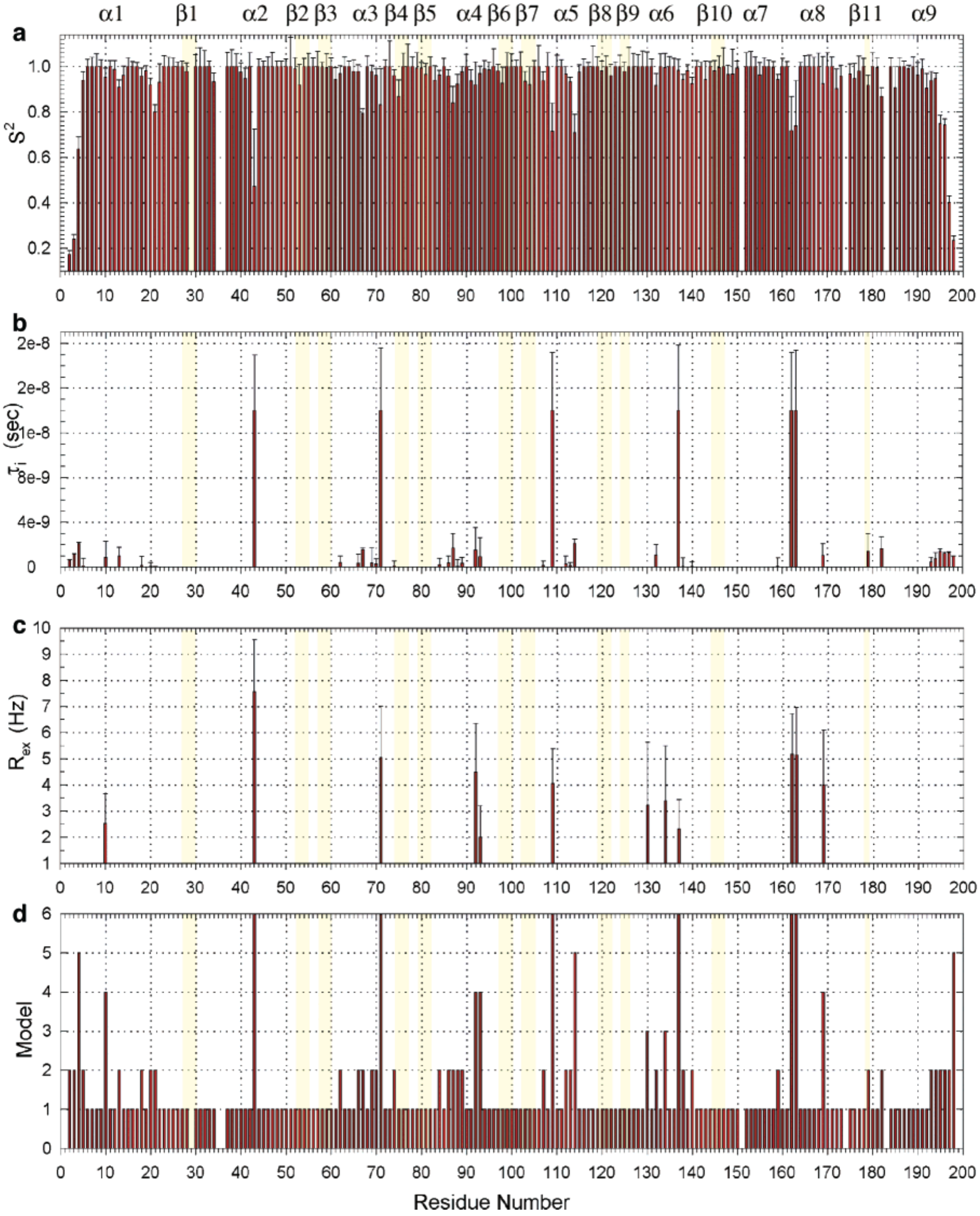

FIGURE 7: Dynamic parameters calculated from the 600 MHz data for each residue of the LC1 molecule assuming a fully anisotropic rotational diffusion tensor. (a) Order parameter S^2. (b) Internal correlation time τ_i (seconds). (c) Exchange contribution R_{ex} (hertz). (d) The model that can account for the measured relaxation rates of each residue is indicated [(1) S^2, (2) S^2 and τ_i, (3) S^2 and R_{ex}, (4) S^2, τ_i, and R_{ex}, (5) S_f^2, S_s^2, and τ_I, and (6) not fitted by models 1−5]. Residues located within defined secondary structure elements are shown in block colors (light blue for α helix and light yellow for β strand). The individual secondary structure elements are labeled at the top.

closer inspection, we observed that within this sheet, residues V28, L53, L75, L98, L120, L145, and L179 have relatively low order parameters compared with the adjacent residues within the same β strand (see also Figure 7a). Including residue V21, which also has a low S^2 value, these eight residues form a concave spine along the larger β sheet face. The hydrophobic side chains of these residues (except for V21) all pack inside the protein core. This concave spine, which exhibits relatively high mobility, is contiguous with residues V20 and A22 that have low S^2 values and is likely important in the hydrophobic interaction of this β sheet face with the γ heavy chain. As most of these residues (V28, L53, L75, L98, L120, L145, and L179) occupy locations characteristic of bulky hydrophobic amino acids within the LRR motifs of LC1, their relatively high mobility may be a common feature of closely related LRR proteins such as U2A′ protein and InIB (*20*, *21*).

The surface opposite β sheet 1 is highly charged, and we previously proposed that this region is involved in ionic interactions with the axonemal protein p45 (*5*). Analysis of

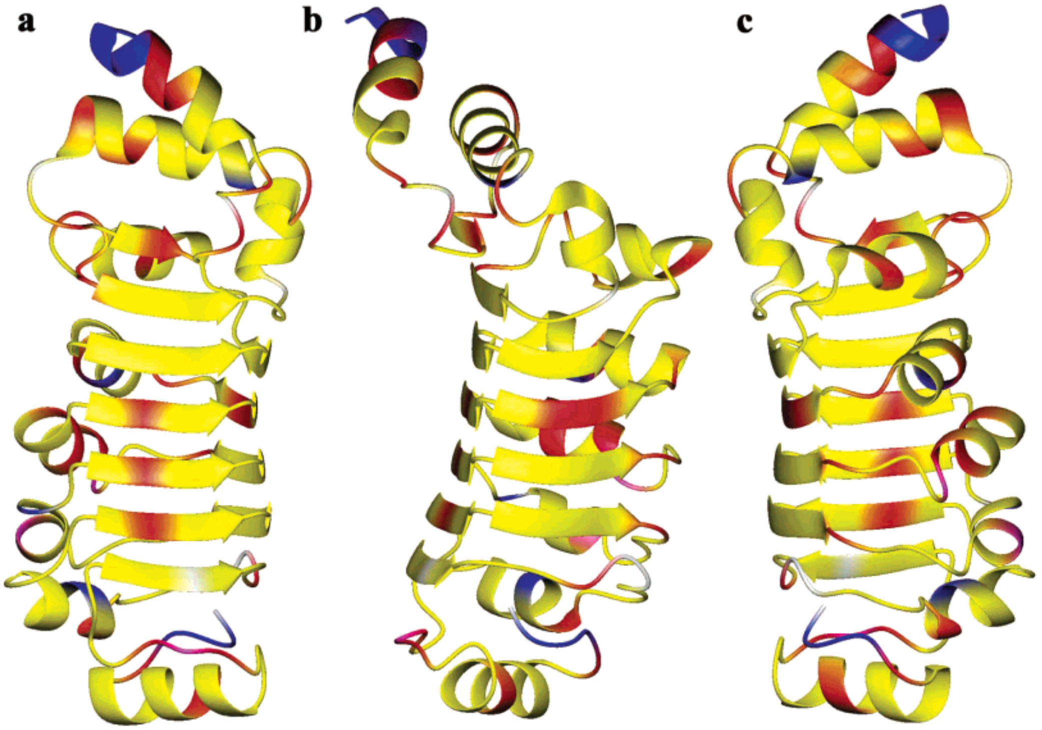

FIGURE 8: Ribbon representations of LC1 colored according to the order parameter S^2 ($1 \geq S^2 > 0.95$, yellow; $0.95 \geq S^2 > 0.85$, red; $0.85 \geq S^2 > 0.75$, magenta; $0.75 \geq S^2 > 0$, blue; and no S^2, white). Most of the residues in sheet 1 (panel a) have almost completely limited high-frequency backbone motion (high order parameters). However, residues V28, L53, L75, L98, L120, L145, and L179, which form an almost continuous stripe through this sheet, exhibit relatively low order parameters and high mobility. Additional regions of higher mobility are evident in panels b and c. The views in panels b and c are rotated 90° and 180° with respect to the *y*-axis of panel a, respectively.

the order parameters for this region revealed a series of charged/polar residues (including T43, E61, K62, S67, K83, E88, S107, S109, and E132) that exhibit lower S^2 values. The high flexibility of these residues may be significant for binding p45. Residue L114 has a very low NOE value and R_2 rate. Both field relaxation data analyses gave very similar nanosecond scale internal correlation times and lower order parameters, and the same model 5 result. Consequently, the average order parameter of helix 5 is much lower than that of the whole molecule. The high mobility of this helical region also may play an important role in ionic interactions with p45. Residues M182 and D185 in the loop region of residues 182−185 have low S^2 values. The high mobility of these residues (and helix 8) significantly influences the orientation of the C-terminal helix 9. As this terminal helix is predicted to insert within the ATP hydrolytic domain of the γ dynein heavy chain, high flexibility of the residues required for its orientation may play a crucial role in the control of dynein motor function. N- and C-terminal residues 2−4 and 195−198, respectively, also have very similar Lipari−Szabo parameters in the two field relaxation analyses (see the Supporting Information). The N-terminal average order parameter is smaller than that of the C-terminal region.

The calculated order parameters for many residues within the central barrel region of LC1 are close to 1.0 (averages of 0.95 and 0.94 for the 600 and 500 MHz data, respectively). Previously, similarly high order parameters have been found for residues in many other proteins such as ribonuclease HI (*23*), δ-ketosteroid isomerase (*24*), barnase (*25*), adipocyte and muscle lipid binding proteins (*26*), Cdc42Hs (*27*), CO-hemoglobin (*28*), and flavodoxin (*29*). In contrast, some other proteins have average values of 0.85−0.90 [e.g., the LC8 dynein light chain (*30*)]. Consequently, there is a significant variation in order parameters detected between different proteins that provides information about the relative flexibility of residues within these distinct molecular systems.

Comparison with Other LRR Proteins. LRR proteins are commonly involved in protein−protein interactions mediated through a concave surface composed of a parallel β sheet that supplies an extensive binding area. For example, the LRR spliceosomal U2A′ protein interacts with a helical region of U2B″ through the concave β sheet surface (*20*). Ribonuclease inhibitor, which consists of 15 LRRs, forms a horseshoe structure that provides a very extensive curved surface for binding ribonuclease A (*31*). Interestingly, the structure of RNase A does not change in the complexed and free states, whereas the cavity of ribonuclease inhibitor is enlarged by ∼2 Å following binding of RNase A and the accumulation of small movements along the chain (*31*). The conformational flexibility of ribonuclease inhibitor suggests that the LRR motif supplies a flexible nonrigid interface for protein−protein interactions. Dynein LC1 is thought to interact with the γ heavy chain via a hydrophobic patch on the concave β sheet surface. The dynamics analysis revealed that residues in this binding region that are conserved in other LRR proteins (i.e., V28, L53, L75, L98, L120, L145, and L179) exhibit relatively high cooperative mobility and could provide an important general feature of the interaction mechanism for this class of proteins.

Significance of Structure Refinement against R_2/R_1 Ratios. Structure refinement using relaxation R_2/R_1 ratios as additional restraints is useful for multidomain and modular proteins where short-range NOE distance constraints are insufficient for precisely defining the relative orientations of the various domains. This approach proved to be very useful to define the orientation of the central barrel and

C-terminal helical domain within LC1 because insufficient long distance restraints were available. Inaccurate long-range order could make the relative orientation of the vectors in different domains of the molecule incorrect and result in an inability to fit all orientations of the vectors to the same model. This inaccuracy was evident from the poor fit to the rotational diffusion tensor in the backbone dynamics analysis. The relaxation-refined structure for LC1 allowed us to obtain a reasonable rotational diffusion tensor as a correct model to perform the dynamic analysis; this was not possible using the initial or control structures. On the basis of the refined structure, we performed a Lipari−Szabo analysis and obtained two sets of highly consistent model-free parameters using 600 and 500 MHz relaxation data.

In conclusion, heteronuclear relaxation measurements have been used as constraints to refine the structure of light chain 1 from the outer dynein arm of *Chlamydomonas* flagella. The C-terminal helix is significantly reoriented by more than 20° compared to the control structure. Furthermore, we analyzed the backbone dynamics of LC1 and identified several regions of relatively high mobility that may be important in defining the mechanism of protein−protein interactions mediated by this dynein component.

ACKNOWLEDGMENT

We thank Sharon Benashski for preparing and characterizing ^{15}N-labeled LC1 protein.

SUPPORTING INFORMATION AVAILABLE

Tables of 500 and 600 MHz relaxation and NOE data for LC1, dynamics parameters derived from the 500 and 600 MHz data sets, and Lipari−Szabo paramaters for the N- and C-terminal residues from the 500 and 600 MHz data sets. This material is available free of charge via the Internet at http://pubs.acs.org.

REFERENCES

1. Karki, S., and Holzbaur, E. L. (1999) *Curr. Opin. Cell Biol. 11*, 45−53.
2. King, S. M. (2000) *Biochim. Biophys. Acta 1496*, 60−75.
3. DiBella, L. M., and King, S. M. (2001) *Int. Rev. Cytol. 210*, 227−268.
4. Benashski, S. E., Patel-King, R. S., and King, S. M. (1999) *Biochemistry 38*, 7253−7264.
5. Wu, H., Maciejewski, M. W., Marintchev, A., Benashski, S. E., Mullen, G. P., and King, S. M. (2000) *Nat. Struct. Biol. 7*, 575−579.
6. Tjandra, N., Garett, D. S., Gronenborn, A. M., Bax, A., and Clore, G. M. (1997) *Nat. Struct. Biol. 4*, 443−449.
7. Lipari, G., and Szabo, A. (1982) *J. Am. Chem. Soc. 104*, 4546−4559.
8. Lipari, G., and Szabo, A. (1982) *J. Am. Chem. Soc. 104*, 4559−4570.
9. Farrow, N. A., Muhandiram, R., Singer, A. U., Pascal, S. M., Kay, C. M., Dish, G., Shoelson, S. E., Pawson, T., Forman-Kay, J. D., and Kay, L. (1994) *Biochemistry 33*, 5984−6003.
10. Kay, L. E., Nicholson, L. K., Delaglio, F., Bax, A., and Torchia, D. A. (1992) *J. Magn. Reson. 97*, 359−375.
11. Markley, J. L., Horsley, W. J., and Klein, M. P. (1971) *J. Chem. Phys. 55*, 3604−3605.
12. Press, S. R., Flannery, B. P., Teukolsky, S. A., and Vetterling, W. T. (1986) *Numerical recipes*, Cambridge University Press, Cambridge, U.K.
13. Kamath, U., and Shriver, J. W. (1989) *J. Biol. Chem. 264*, 5586−5592.
14. Palmer, A. G., Rance, M., and Wright, P. E. (1991) *J. Am. Chem. Soc. 113*, 4371−4380.
15. Cordier, F., Caffrey, M., Brutscher, B., Cusanovich, M., Marion, D., and Blackledge, M. (1998) *J. Mol. Biol. 281*, 341−361.
16. Dosset, P., Hus, J.-C., Blackledge, M., and Marion, D. (2000) *J. Biomol. NMR 16*, 23−28.
17. Hus, J.-C., Marion, D., and Blackledge, M. (1999) *J. Am. Chem. Soc. 121*, 2311−2312.
18. Pearlman, D. A., Case, D. A., Caldwell, J. C., Seibel, G. L., Singh, U. C., Weiner, P., and Kollman, P. A. (1991) *AMBER 4.0*, University of California, San Francisco.
19. Maciejewski, M. W., Liu, D., Prasad, R., Wilson, S. H., and Mullen, G. P. (2000) *J. Mol. Biol. 296*, 229−253.
20. Price, S. R., Evans, P. R., and Nagai, K. (1998) *Nature 394*, 645−650.
21. Marino, M., Braun, L., Cossart, P., and Ghosh, P. (1999) *Mol. Cell 4*, 1063−1072.
22. Blackledge, M., Cordier, F., Dosset, P., and Marion, D. (1998) *J. Am. Chem. Soc. 120*, 4538−4539.
23. Mandel, A., Akke, M., and Palmer, A. (1995) *J. Mol. Biol. 246*, 144−163.
24. Yun, S., Jang, D., Kim, D., Choi, K., and Lee, H. (2001) *Biochemistry 40*, 3967−3973.
25. Sahu, S., Bhuyan, A., Udgaonkar, J., and Hosur, R. (2000) *J. Biomol. NMR 18*, 107−118.
26. Constantine, K., Friedrichs, M., Wittekind, M., Jamil, H., Chu, C., Parker, R., Goldfarb, V., Mueller, L., and Farmer, B. (1998) *Biochemistry 37*, 7965−7980.
27. Loh, A., Guo, W., Nicholson, L., and Oswald, R. (1999) *Biochemistry 38*, 12547−12557.
28. Volkman, B., Alam, S., Satterlee, J., and Markley, J. (1998) *Biochemistry 37*, 10906−10919.
29. Liu, W., Flynn, P., Fuentes, E., Kranz, J., McCormick, M., and Wand, A. (2001) *Biochemistry 40*, 14744−14753.
30. Fan, J. S., Zhang, Q., Tochio, H., and Zhang, M. (2002) *J. Biomol. NMR 23*, 103−114.
31. Kobe, B., and Deisenhofer, J. (1993) *Nature 366*, 751−756.

BI026762J